Optimization of Fabrication Conditions and Calibration of Polyvinylidene Fluoride for use as a Biosensor

A Thesis

SUBMITTED TO THE FACULTY OF THE UNIVERSITY OF MINNESOTA-DULUTH

BY

Matthew Danley

IN PARTIAL FULFILLMENT OF THE REQUIREMENTS

FOR THE DEGREE OF

MASTER OF SCIENCE

Advisor:

Victor K. Lai, Ph.D.

Committee Members:

Richard Davis, Ph.D.

Ping Zhao, Ph.D.

August 2022

Acknowledgments

I would like to thank my advisor, Dr. Victor Lai, of the Chemical Engineering department at the University of Minnesota-Duluth. He was always available for questions regarding research, homework, and guidance on my academic career. His patience this past school year was very much appreciated.

I would also like to thank my committee members Dr. Richard Davis and Dr. Ping Zhao. Their expertise was invaluable in solving issues during experimentation. Without their help, I would not have been able to graduate this summer.

I would like to thank my fellow research group members, Jack Kloster, and Tony Stunz for their work and support on this project. Without them, I would not have been able to finish this project. I would like to thank other group members for their ongoing support in Dr. Lai's research group, Elizabeth B. and Sonia L. You all made being a part of this research group an enjoyable experience!

I would like to thank Mike Danley and George Behr for their assistance with designing and building the flow chamber. Their insight allowed for a simple design and build for experiments.

Finally, I would like to thank my family for their unwavering support during my time at Duluth. Words cannot describe how important their encouragement and support was these past seven years, thank you!

Abstract

The Transcatheter Aortic Valve Replacement (TAVR) is a minimally invasive procedure that utilizes a catheter to deploy a replacement valve in patients with valve stenosis. Although TAVR has lowered the risk of some complications, such as in-hospital mortality rates, there are documented increases in complications compared to open heart surgery, such as increasing numbers of pacemaker implantation after the procedure. The underlying mechanisms of these complications have not been identified. It is thought that 3D printing a replica of a patient's aorta would allow for flow shear stress analysis, pressure compressive tests, and investigation of cyclic distension of the aortic walls. Polyvinylidene fluoride is a piezoelectric polymer that is a promising material to be used as a sensor to detect the shear stress, compressive forces, and distension inside the aorta model. Porous PVDF membranes have been shown to have higher piezoelectric properties compared to nonporous PVDF. It is thought the increase in porosity leads to a greater deformation, and in turn, a larger piezoelectric response to mechanical stresses.

The goals of this study are to optimize the fabrication process of porous PVDF membranes using ZnO nanoparticles to induce pores and to design and build a flow chamber to then calibrate the PVDF membranes to physiological conditions. One issue identified in the fabrication process has been the removal of ZnO nanoparticles. The ZnO nanoparticles were added to a solution of PVDF and 2-butanone, cast and dried on a petri dish. 1cm by 1cm squares were cut from the PVDF membranes, weighed, and then placed in a hydrochloric acid bath. The HCl dissolved ZnO, which then diffused out of the membrane as $ZnCl_2$. The mass of the membrane was measured at various time points while in the acid bath. These measurements were used to model the diffusion of $ZnCl_2$ out of the membrane. The removal of ZnO was predicted to follow a shrinking core assumption, or a unimolecular diffusion of $ZnCl_2$. The effective diffusivity of $ZnCl_2$ was calculated for PVDF/ZnO membranes at 10%, 20%, 30%, and 40% wt ZnO as well as for 35-45nm, 80-200nm, and 500nm particle sizes. The effective diffusivities increased from 20% wt ZnO and peaked at 40% wt ZnO and decreased as the particle sizes increased from 35-45nm to 500nm. Further studying the porosity and tortuosity of PVDF membranes would allow for calculation of the diffusion coefficient of $ZnCl_2$ out of the PVDF matrix.

A flow chamber was built to calibrate PVDF membranes at physiological conditions in the aorta. 1" diameter tubing was used as the aorta segment and a submersible pump generate pressure and flow in the flow chamber. The voltages from the PVDF sensors were collected under varying flow rates (150mL/s – 400mL/s) and varying pressures (5mmHg to 30mmHg). The flow chamber mimicked the physiological flow rates of the aorta but did not mimic physiological pressure. The PVDF sensors generated decreasing signal as pressure and flow rates increased, which was not expected. Going forward, increasing the pressure in the flow chamber should allow for calibration of PVDF membranes under forces similar to those seen in the aorta.

Table of Contents

List of Figures

List of Abbreviations

Abbreviation	Description
TAVR	Transcatheter Aortic Valve Replacement
SAVR	Surgical Aortic Valve Replacement
PVDF	Polyvinylidene Fluoride
Wt%	Weight Percent

Chapter 1) Introduction

1.1) Transcatheter Aortic Valve Replacement Procedure

The transcatheter aortic valve replacement (TAVR) procedure is a minimally invasive medical treatment option for patients with heart valve stenosis [1,2]. Heart valve stenosis, a condition in which heart valves narrow, reduces or blocks blood flow from the aorta to the rest of the body [3–5]. When the aortic valve does not fully open, this increases the pressure in the main chamber in the heart, and the heart can compensate by thickening its wall to maintain pressure, which leads to deterioration of function[2]. Examples of heart valve stenosis are shown in Figure 1 below. While some patients can have heart valve stenosis treated with medication, severe cases require further treatment, such as valve replacement[2]. The TAVR procedure is an option for patients that can not undergo open heart surgery[1,2,6,7]. Figure 2 shows how the valve is deployed using a catheter[8].

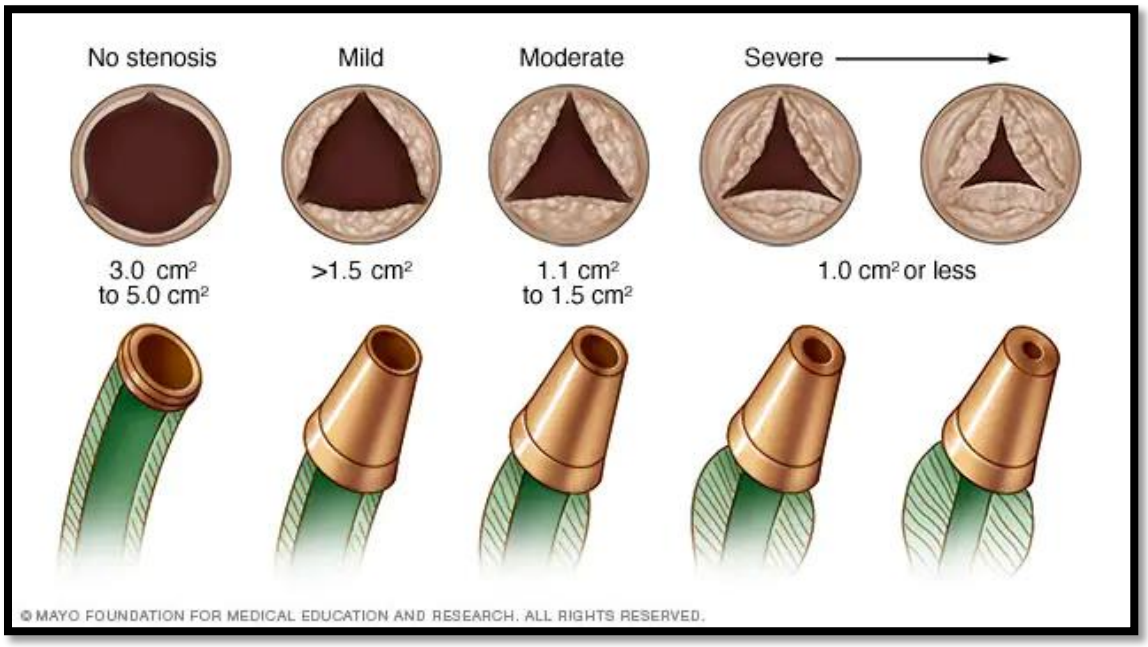

Figure 6. Heart Valve Stenosis. The different stages of heart valve stenosis are shown with comparisons to a hose. As the condition worsens, the valve becomes more narrowed, which increases pressure[3].

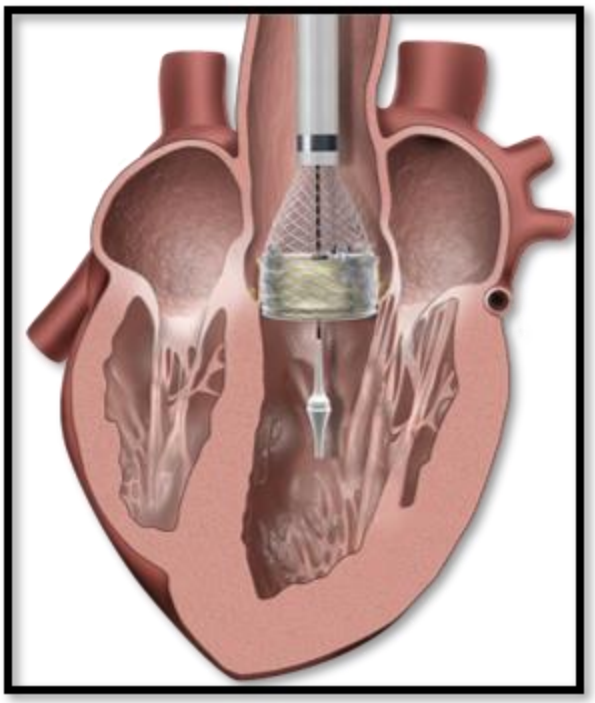

Figure 7. Replacement Valve Deployment during a TAVR procedure. A catheter is used to maneuver the replacement valve into proper position[8].

TAVR can be an excellent option for many patients as it had a lower rate of some complications. These include in-hospital mortality rates, cumulative 30-day mortality rates, and 90-day post-discharge mortality rates declined[6]. Even though TAVR is minimally invasive, studies have shown there could be several complications post-procedure[6,9,10]. Despite the declining complication rates, the 90-day mortality rate was nearly double the rate for open heart surgery[6]. This is concerning and counterintuitive, that the open-heart surgery procedure had a lower 90-day mortality rate compared to a minimally invasive procedure solving the same condition. Another example is the increase in the number of post-operation TAVR patients being admitted into the hospital again for a permanent pacemaker implantation[11]. These examples suggest an underlying mechanism in the complications. One possible cause of complications could be that the replacement valve changes the blood flow environment in the aorta. The replacement valve could alter the flow pattern or pressure in the aorta, which could alter the mechanical microenvironment of the surrounding tissue, thus altering cellular behavior[12]. Since patients who undergo TAVR compared to SAVR are either chosen for a clinical trial or are considered high risk for open heart surgery [2], subjecting a patient to invasive monitoring post-procedure would not be feasible. Instead, in vitro studies of changes in pressure and flow should be conducted.

Hence the overall goal of this research project is to study complications of the TAVR procedure in vitro using three-dimensional printed aorta models to monitor flow and pressure within the aorta before and after a TAVR implant. Other studies have shown that it is possible to create an environment that mimics that of the aorta [13–15]. For

example, Zelis et al successfully printed a 3D model for a specific patient but were unable to replicate the pressure versus flow relationships[15]. Valverde successfully printed a 3D model of a transverse aortic arch that was not statistically different from dimension measurements taken from the MRI and X-ray angiography[13]. These studies show that designing and printing a 3D model of the aorta to study the effects of TAVR is possible and promising.

1.2) Polyvinylidene Fluoride Piezoelectric Polymer

To achieve our goal of quantifying the flow characteristics and mechanical deformations within the aorta, a biosensor that can be embedded within the aortic segment is needed. One promising material for use in the sensor is polyvinylidene fluoride (PVDF). PVDF is a piezoelectric polymer that has many applications, including use as a sensor [16]. PVDF is a piezoelectric material since it is a polarized polymer. The monomer of PVDF is 1,1-difluoroethylene. PVDF is polarized due to the large difference in electronegativities of the fluorine and hydrogen atoms in the monomer. The PVDF polymer chain alternates between fluorine and hydrogens attached to the carbon backbone, illustrated in Figure 3. When the polymer chain is subjected to a mechanical force, the distance between the fluorine and hydrogen atoms changes, which leads to a change in polarization. This can be measured as a voltage. This change in voltage is proportional to the change in mechanical stress, as more force is applied, a large change in voltage is generated.

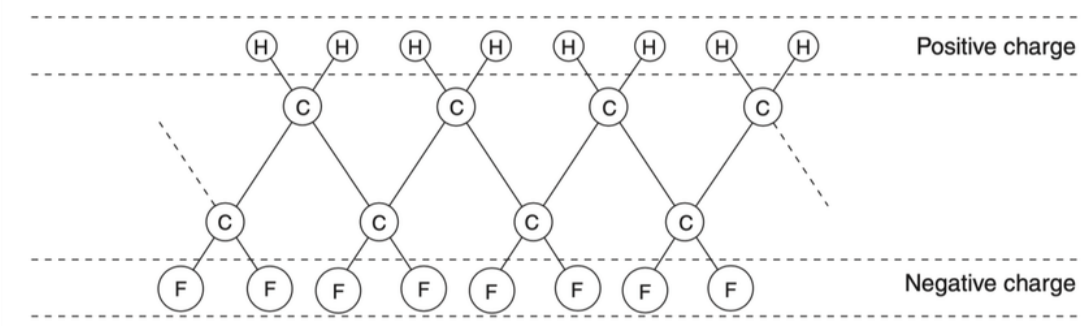

Figure 8. PVDF Polymer Chain. The polymer of PVDF with Hydrogen atoms on one side of the carbon chain and Fluorine atoms on the other side of the carbon chain with respective relative charges[17].

Various studies have shown the viability of PVDF as a sensor. For example, Li et al used a PVDF membrane to measure the velocity of turbulent wind[18]. Chen-Glasser et

al details many different applications of PVDF including as biomechanical energy harvesting systems, sensors, and wound scaffolds[19]. Takashima et al suggests that PVDF could be used as a sensor for bedridden patients[20].PVDF has been used as a sensor for human voice detection, hand motion, breathing rate, wrist pulse, arterial pressure pulse, and heartbeat detection[19,21]. Other studies have used PVDF to monitor blood pressure and flow, such as McLaughlin et al using PVDF to determine the arterial pulse wave velocity[22].

For studying the complications of the TAVR procedure, the PVDF sensor needs to be thin but sensitive. The sensor needs to be able to detect small changes in flow and pressure before and after the valve is implemented. Since the goal of the overall project is to study the effects of the implantation of the valve, the sensor needs to be thin enough to not disrupt flow patterns, but sensitive enough to detect small changes in pressure and flow. PVDF is an ideal material since it has a high piezoelectric constant (that it generates a large voltage in response to a mechanical stress) and is flexible[23]. In addition, studies have shown that inducing pores into a PVDF membrane can increase its piezoelectric properties [23–26]. It is thought that the induction of pores allows the PVDF polymer chain to flex more, generating more polarization, which leads to an increase in voltage[23,24,26]. This means that the PVDF sensor to be used for studying the TAVR complications could be porous, it would be advantageous to get a larger signal when looking at small changes in mechanical applied forces.

Many groups have used zinc oxide (ZnO) nanoparticles to induce additional pores into a PVDF membrane[23,24,26]. These porous PVDF membranes were fabricated by the protocol outline in Mao et al[23]. PVDF was dissolved in 2-butanone, and various amounts of ZnO nanoparticles were added to the solution[23]. The solution was then mixed to ensure homogeneity, then cast and dried[23]. Placing the PVDF/ZnO solid membrane into a Hydrochloric acid bath etched away the ZnO nanoparticles and left behind a porous PVDF membrane[23]. Tucker et al[24] and Danley[26] reported that not all the ZnO nanoparticles were removed through this process. This could alter the structure and properties of the PVDF sensor, so optimizing the removal of ZnO nanoparticles is of interest for this study.

1.3) Specific Goals of this Research

The two objectives of this specific research project are

1) to optimize the fabrication of the PVDF sensors. In a previous study[26], there were problems removing the zinc oxide nanoparticles from the PVDF structure. One variable that has not been extensively studied was how the ZnO nanoparticles diffuse out of the PVDF membrane while in the acid bath. To optimize the fabrication process, modeling the diffusion and calculating the diffusion coefficient of ZnO out of PVDF would improve further production of PVDF sensors.
2) design and build a flow chamber to calibrate the PVDF membranes. Before placing the PVDF sensors in a 3D printed silicone model of the aorta, the sensor needs to be calibrated to conditions seen in the aortic segment. A flow chamber needs to be built that mimics conditions of the aorta so the PVDF sensor can be calibrated to blood flow rates and blood pressures experienced in the aorta artery.

Chapter 2) Modeling the Diffusion of $ZnCl_2$ out of PVDF Membranes

2.1) Introduction

Inducing additional pores into a PVDF membrane during the fabrication process has been studied, but not fully optimized for use as a biosensor [23–29]. Previous studies using PVDF as a biosensor resulted in lower piezoelectric signals[24,26] than expected[30]. One variable that has not been studied is the removal of the ZnO nanoparticles during the acid bath etching process. It is possible that having some ZnO nanoparticles in the PVDF membranes negatively affects the piezoelectric output.

The mass transport through PVDF has been well studied since PVDF is used as a filtering membrane [31–34] but not specifically for ZnO diffusing out of PVDF membranes during the fabrication process. Ardeshiri et al fabricated PVDF membranes with ZnO nanoparticles for use in membrane distillation[34]. These ZnO nanoparticles were left in to see their effects on diffusion in a PVDF membrane[34]. Ardeshiri et al found that adding ZnO nanoparticles to the PVDF membranes altered the flux of salt (NaCl) water through the membrane[34]: the average flux of the 0.25% and 0.5% ZnO membranes was higher than pure PVDF and decreased with increasing amounts of ZnO nanoparticle contents[34]. They speculate that the differences may be from the phase inversion exchange rate during fabrication[34]. This suggests that leaving ZnO nanoparticles in the membrane alters the porosity, thus affecting the flux of salt water.

These findings from Ardeshiri et al suggest that varying the amounts of ZnO nanoparticles in the membranes could affect the diffusion of zinc out of the PVDF matrix. One problem encountered in a previous study [26] regarding removing ZnO was that most of the nanoparticles were removed quickly during the acid bath at the start, while minimal amounts were removed even when the membranes were left in the bath for longer times. Modeling the diffusion of the nanoparticles from the membrane would help understand the transport properties, and possibly improve the piezoelectric properties of the PVDF sensor.

When the PVDF/ZnO membranes are placed into the HCl acid bath, a chemical reaction takes place. The reaction is outlined in equation 1.

$$ZnO(s) + 2HCl(l) \longrightarrow ZnCl_2(l) + H_2O(l) \quad (1)$$

where two moles of HCl acid reacts with one mole of ZnO, with the products $ZnCl_2$ and H_2O. The removal of ZnO nanoparticles depends on the diffusion of the $ZnCl_2$ molecules out of the PVDF matrix. The diffusion occurs because the concentration of $ZnCl_2$ in the membrane is larger than the $ZnCl_2$ concentration in the acid bath outside the membrane. Assuming the HCl can penetrate the PVDF membranes very quickly, and that the reaction rate is almost instantaneous compared to the time for diffusion of the $ZnCl_2$ out of the membrane, the diffusion can be described as unimolecular through the solvent.

Another assumption regarding the ZnO nanoparticle removal process is that the nanoparticles on the surface react and dissolve first, and particles in the center of the membrane react and dissolve later - this is known as the shrinking core model[35]. The shrinking core model describes when a solid particle is being removed from a system and the amount of the solid is "shrinking" or decreasing[35]. In this case, since the ZnO nanoparticles are assumed to be homogenous throughout and are dissolved instantaneously to $ZnCl_2$, a layer of $ZnCl_2$ must be removed before the HCl can penetrate deeper into the membrane. This process is shown in Figure 4 below. The flux of $ZnCl_2$, N_{ZnCl2}, is shown leaving the membrane, with a moving boundary layer towards the center of the PVDF membrane. The position of the moving boundary layer is defined as z, which increases the closer the boundary layer gets to the center. C_b is the bulk molar concentration of ZnO (or $ZnCl_2$), molecules in the membrane, which remains approximately constant throughout the removal process since the nanoparticles are assumed to be homogenous within the membrane. C is the total liquid molar concentration in the acid bath, which also remains approximately constant since the bath is essentially an infinite source of concentrated HCl.

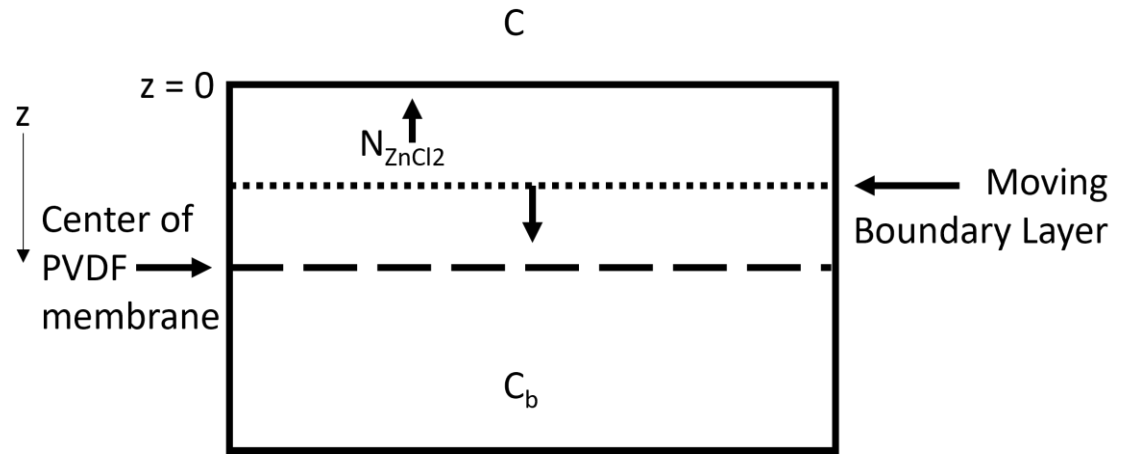

Figure 4. Diffusion of $ZnCl_2$ Out of PVDF membrane. The black square represents the PVDF membrane in the acid bath. The large dashed line represents the center of the PVDF membrane. The smaller dash line shows the boundary layer moving from the top of the membrane towards the center line. The direction of flux, N_{ZnO} is shown leaving the PVDF membrane. Cb refers to the bulk molar concentration of ZnO nanoparticles in the membrane with the volume shrinking as the boundary layer moves inward. C refers to the total liquid molar concentration, which stays constant throughout the experiment.

2.2) Materials and Methods

The PVDF membranes were fabricated using the protocols outlined in [23,24,26]. Briefly, PVDF powder (Alfa Aesar, Ward Hill, MA) was dissolved in 2-butanone solvent (Alfa Aesar, Ward Hill, MA) at 80°C. Three different sizes of ZnO nanoparticles of 35-45nm, 80-200nm, and 500nm respectively were added to the solution (US Research Nanomaterials, Houston, TX). The mixture was placed in an ultrasonication bath for 30 minutes and vortexed to ensure a homogenous solution. The PVDF/ZnO solutions were poured into 40mL glass Petri dishes and dried in an oven at 80°C. Various amounts of ZnO nanoparticles were added to each PVDF solution to create different weight percent ZnO membranes of 10, 20, 30, and 40 wt%. The effects of weight percent ZnO on $ZnCl_2$ diffusion were studied using the 35-45nm particle sizes, while the effects of particle sizes were studied using 40 wt% ZnO samples.

The PVDF/ZnO sample masses were collected once the 2-butanone was fully evaporated. The membranes were then placed in an 11.65M HCl acid bath and pulled out at various times for analysis. To measure the weight of the samples at different time points, the samples were pulled out, rinsed off, and allowed to dry before weighing again. The samples were placed in the acid bath for six hours, and their weights were measured at the 5-, 10-, 15-, 20-, 30-, 40-, 50-, 60-, 90-, 120-, 240-, and 360-minute marks.

Once the masses of the membranes were collected, the mass of PVDF and ZnO could be calculated at each time point. The mass of the ZnO at each time point, m_{ZnO}, in the membrane was calculated using the wt% of each membrane:

$$m_{ZnO} = m_{Sample} * wt\%ZnO \quad (2)$$

Where m_{sample} is the mass of the entire sample taken experimentally at each time point. The fraction of ZnO removed at each time point, y_{ZnO}, was calculated by using the following equation:

$$y_{ZnO} = \frac{m_{ZnO_i} - m_{ZnO}}{m_{ZnO_i}} \quad (3)$$

Where m_{ZnOi} is the initial mass of ZnO in the sample. It is assumed that this removal process is limited by the diffusion of $ZnCl_2$ out of the membrane, i.e., HCl penetrates through the membrane instantaneously and dissolves all the ZnO into $ZnCl_2$, such that the initial concentration of $ZnCl_2$ is equal to the concentration of ZnO nanoparticles inside the membrane after fabrication.

2.3) Unimolecular Model Derivation

The mass balance of $ZnCl_2$ in this system is:

$$Accumulation\ Rate = Rate\ In - Rate\ Out + Rate\ of\ Generation \quad (4)$$

It is assumed that all the ZnO is converted to $ZnCl_2$ instantaneously in the membrane at the start of the acid bath, no $ZnCl_2$ is being generated throughout the experiment, and no additional $ZnCl_2$ is entering the membrane during this experiment. Therefore, equation 4 can be simplified to equation 5.

$$AccumulationRate = -RateOut \quad (5)$$

The accumulation of $ZnCl_2$ in the membrane is the rate of change of $ZnCl_2$ in the membrane (equation 6). The change of moles of $ZnCl_2$, n, per time can be calculated from the concentration of $ZnCl_2$, C_b:

$$Accumulation\ Rate = \frac{dn}{dt} = \frac{d(C_b V)}{dt} = \frac{C_b d(Az)}{dt} = C_b A \frac{dz}{dt} \quad (6)$$

Where *A* is the area of the PVDF membrane. The rate of removal of $ZnCl_2$ can be written in terms of its flux, N_{ZnCl2}.

$$Rate\ Out = Area * FluxZnCl_2 = AN_{ZnCl_2} \quad (7)$$

The total flux of $ZnCl_2$ will be the fraction of the flux moving in the membrane minus the fraction of $ZnCl_2$ already dissolved and removed from the membrane.

$$N_{ZnO} = X_s N_{ZnO} - CD_e \frac{dX_s}{dz} \quad (8)$$

With X_s the fraction of ZnO, *C* the total liquid molar concentration, D_e the effective diffusivity of $ZnCl_2$ through the PVDF membrane, and *z* the position of the moving boundary layer. Equation 8 can be rearranged to the following differential equation:

$$\frac{dX_s}{dz} = \frac{N_{ZnCl_2}}{\frac{-CD_e}{(1 - X_s)}} \quad (9)$$

The mass fraction of $ZnCl_2$ is assumed to be zero at the surface of the PVDF membrane, which is defined at $z = 0$ in Figure 4. Equation 9 can be solved by integrating from $z = 0$ to $z = z$, and from $x_s = 0$ to $x_s = x_b$, the bulk fraction, to yield equation 10.

$$N_{ZnCl_2} = \frac{D_e C}{z} ln\left(\frac{1}{1 - x_b}\right) \quad (10)$$

Equation 6 and equation 10 can be substituted into equation 5 to generate a differential equation that describes the change in boundary layer position with time:

$$C_b A \frac{dz}{dt} = A \frac{D_e C}{z} ln\left(\frac{1}{1 - x_b}\right) \quad (11)$$

The position of the boundary layer is at the surface of the membrane, $z = 0$, at the beginning of the experiment at $t = 0$. This boundary condition, $z = 0$ at $t = 0$, can be used to solve the differential in equation 11. The bulk fraction, x_b can be experimentally

calculated setting $x_b = C_b/C$, the ratio of the bulk concentration and total liquid concentration.

$$z = \sqrt{2D_e t \frac{C}{C_b} ln\left(\frac{C}{C - C_b}\right)} \tag{12}$$

Equation 12 models the expected position of the moving boundary layer inside the PVDF membrane at any given time. To fit our experimental data to this model, Equation 12 can be linearized to equation 13.

$$z^2 = \left(2D_e \left(\frac{C}{C_b}\right) ln\left(\frac{C}{C - C_b}\right)\right) t \tag{13}$$

Equation 13 can be used to determine the fit of the experimental position of the boundary layer and the model calculated position of the boundary layer. Plotting the experimental position of the moving boundary layer squared against time should result in a straight line when the $ZnCl_2$ is diffusing out of the PVDF membrane. The slope of that line is equal to $\left(2D_e \left(\frac{C}{C_b}\right) ln\left(\frac{C}{C-C_b}\right)\right)$, which can be used to determine the effective diffusivity of $ZnCl_2$ out of the membrane.

The experimental position of the moving boundary layer, $z_{experimental}$, was determined using the fraction removed, y_{ZnO}, and thickness of the membrane, T.

$$z_{experimental} = y_{ZnO} T \tag{14}$$

2.4) Result

2.4.1) Effects of Wt% ZnO on Diffusion

The fraction of ZnO removed, $y_{ZnO,}$ was calculated at each time interval using Equation 3, and the comparisons for the different wt% ZnO membranes are shown in Figure 5 below.

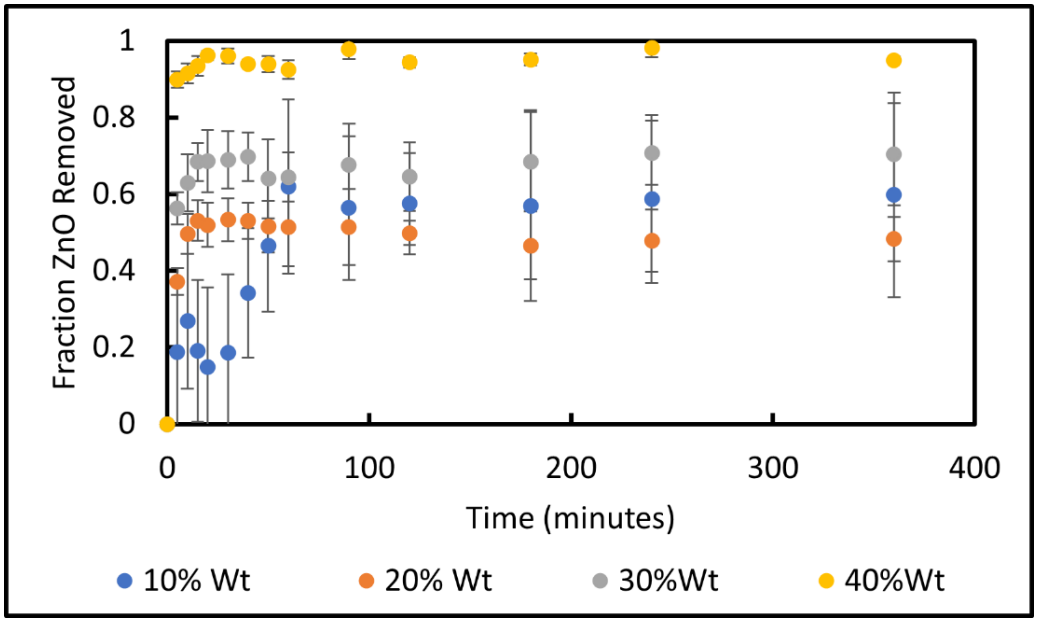

Figure 5. Fraction ZnO Removed Over Time at Various Wt% ZnO. Each data point represents the average fraction of ZnO removed for four replicates from each wt% ZnO, with the error bars representing the standard deviation.

For all the wt% ZnO samples, minimal amounts of ZnO were removed from the membranes after 60 minutes in the acid bath. This means most of the diffusion of $ZnCl_2$ occurred almost immediately, which is illustrated clearly by the 40% wt ZnO samples in Figure 5. After 60 minutes, the fraction of ZnO removed reached a plateau, yet these values for the plateau were different from each other. This is shown in Figure 6.

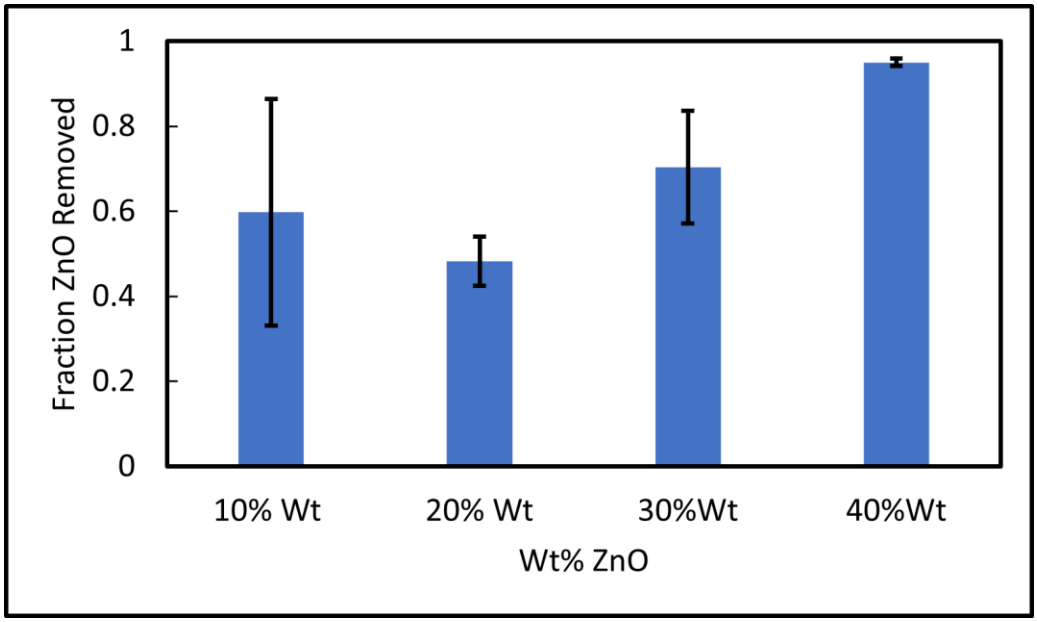

Figure 6. Average Final Fraction ZnO Removed at Various Wt% ZnO. Error bars represent the standard deviation of 4 replicates of each sample.

Figure 6 shows the average final fraction of ZnO removed at various wt% ZnO. The largest fraction removed was the 40%wt ZnO sample with an average of 95% of the ZnO nanoparticles removed. The smallest amount of ZnO removed was 48% for the 20%wt ZnO samples. There was an increase in fraction removed from 20% up to 40% wt ZnO samples. The 10% wt ZnO sample had a larger fraction removed compared to the 20% samples, however, the variation between the four replicates was very large, with an average fraction removed of 59% but a standard deviation of 26%. The increase in fraction of ZnO removed with an increase in wt% ZnO suggests that when more ZnO is added during the fabrication process, more can be dissolved and diffuse out of the membrane.

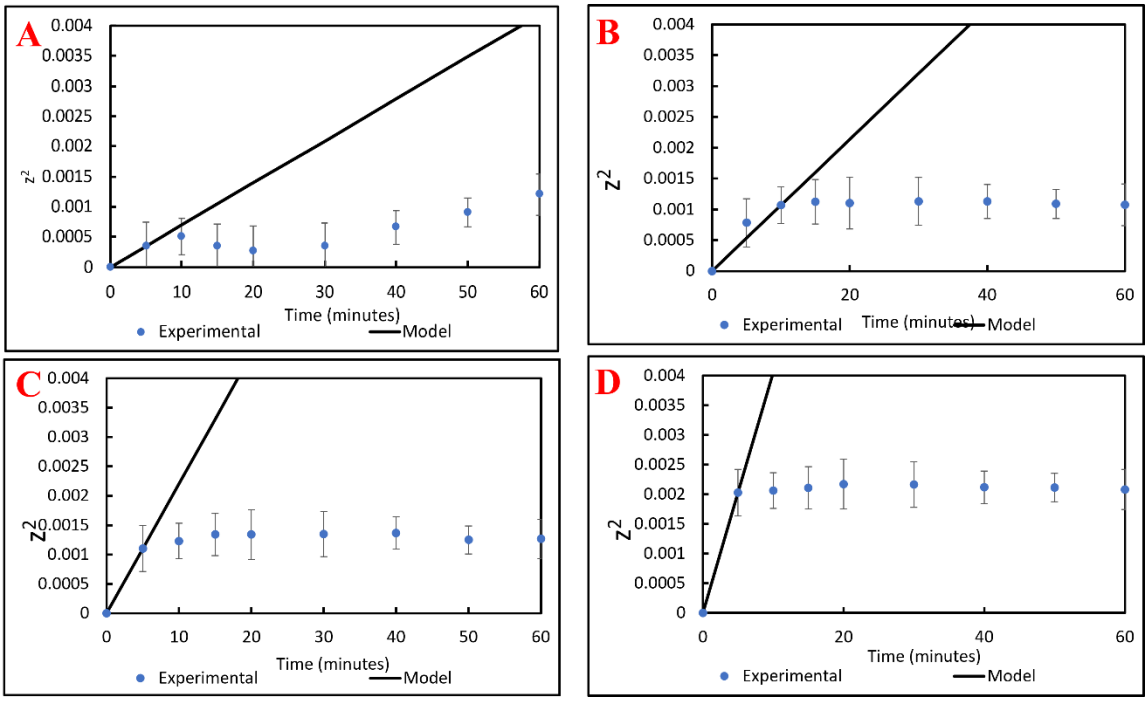

Figure 7. Experimental and Model Position of Moving Boundary Layer for Various Wt% ZnO Samples. A) The squared experimental moving boundary layer position of 10% Wt ZnO, with the black line representing the slope of the model equation. B) The squared experimental moving boundary layer position of 20% Wt ZnO, with the black line representing the slope of the model equation. C) The squared experimental moving boundary layer position for 30% wt ZnO, with the black line representing the slope of the model equation. D) The squared experimental moving boundary layer position for 40% wt ZnO, with the black line representing the slope of the model equation. Each data point represents the average of four replicate trials, with error bars representing the standard deviation.

The experimental moving boundary layer position was calculated using equation 13. Figure 7A, B, C, and D show the plots of z^2 *vs t* based on equation 13 for 10%, 20%, 30%, and 40% wt ZnO samples respectively. The slope of the model was calculated using

only the data at the 5-minute interval since most of the ZnO nanoparticles were removed after 5 minutes in the acid bath.

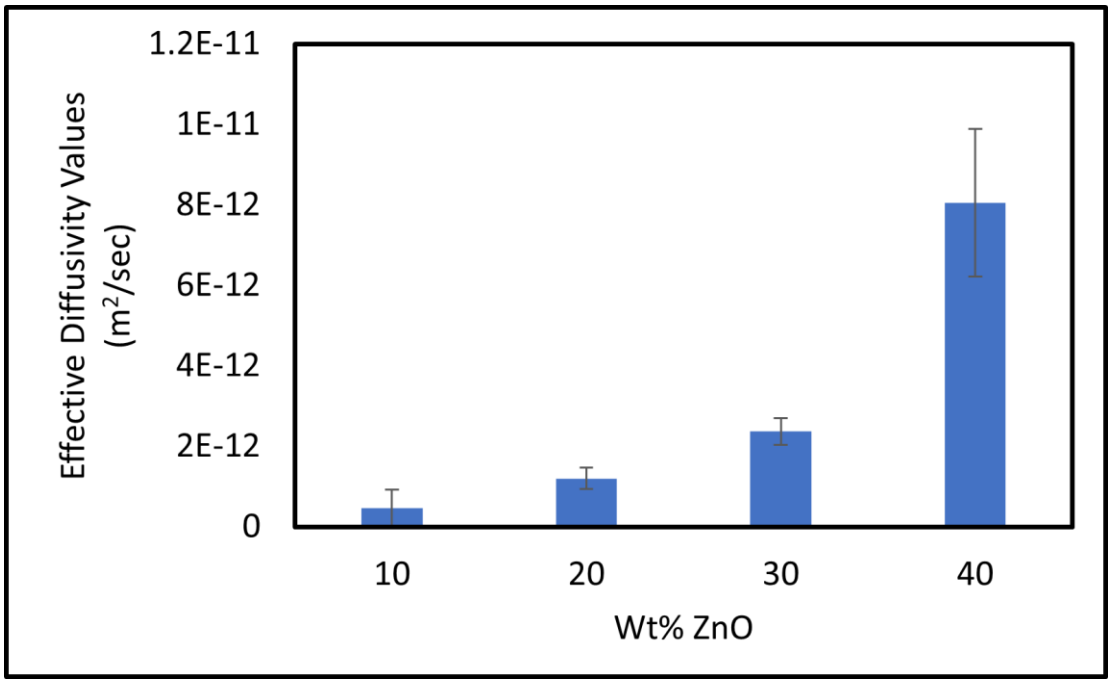

Figure 8. Effective Diffusivity of $ZnCl_2$ molecules through PVDF membranes of various wt% ZnO samples. The effective diffusivity of various wt% ZnO samples were calculated by using the slope of the model in figures 7A, B, C, and D. Each bar represents the average effective diffusivity of four replicates with errors bars representing standard deviations.

The effective diffusivities were calculated using the slope of the model line in Figures 7A, B, C, and D. The effective diffusivity increased as the wt% ZnO was increased in each sample. This suggests that the diffusion of $ZnCl_2$ occurs faster in higher wt% ZnO samples since the higher wt% ZnO samples would leave more pores and channels for the $ZnCl_2$ to diffuse out of after being placed in the acid bath. However, since the model was calculated using only a few data points, the diffusion coefficient cannot be estimated with certainty.

2.4.2) Effects of ZnO Nanoparticle Size on Diffusion

Figure 9 shows the fraction of ZnO nanoparticles removed from the PVDF membrane using different particle sizes (at 40wt% ZnO in all cases). The fraction of ZnO removed for the smallest particle size, 35-45nm, increased rapidly, and plateaued after 30 minutes in the acid bath. The fraction removed for 80-200nm sized particles was more

gradual compared to the 35-45nm particle size. The fraction removed for the 500nm sized particles plateaued after about 1 hour in the acid bath.

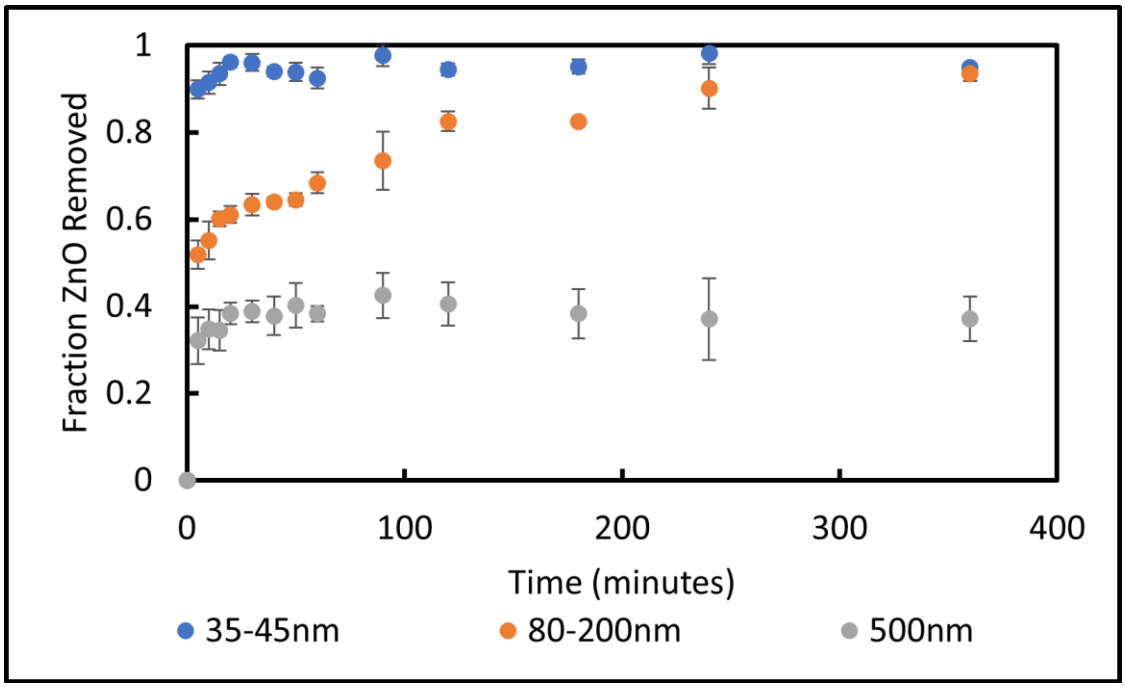

Figure 9. Fraction of ZnO Removed over Time using various particle sizes. Each data point represents an average of n=4 for 35-45nm, and n=3 for 80-200nm and 500nm samples. The error bars represent the standard deviations between replicates.

The average final fraction of ZnO removed values are shown in Figure 10. The largest average fraction removed was the 35-45nm samples, followed closely by the 80-200nm samples. The largest particle size, 500nm, had the lowest fraction of ZnO removed from the membrane.

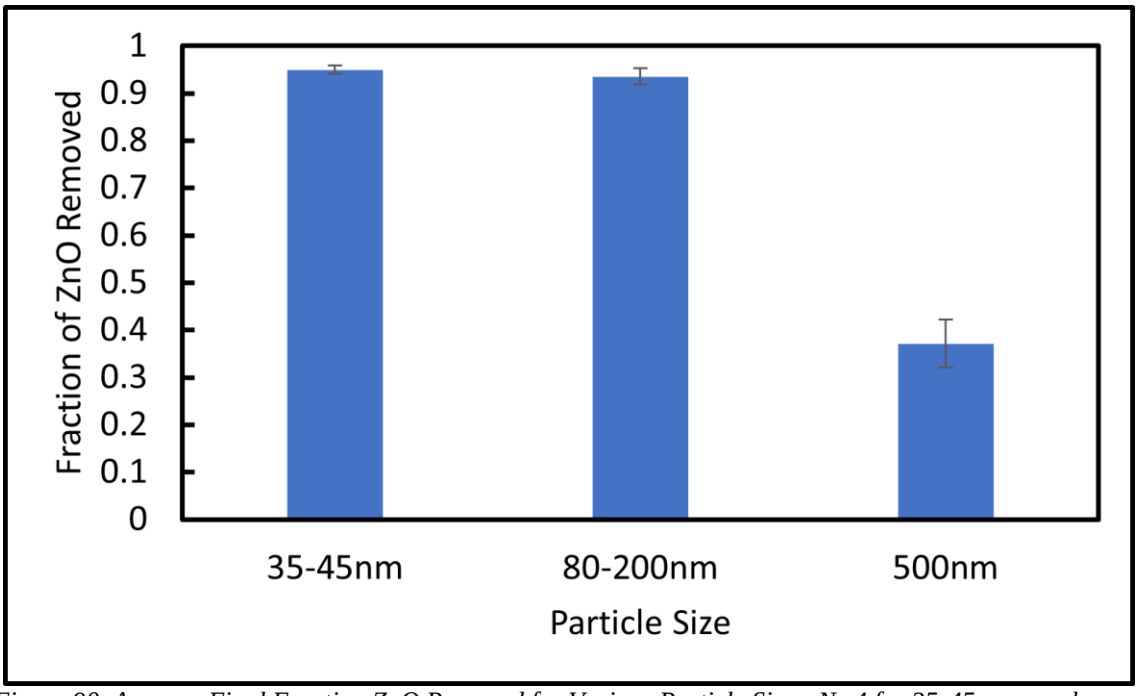

Figure 90. Average Final Fraction ZnO Removed for Various Particle Sizes. N=4 for 35-45nm samples, n=3 for 80-200nm and 500nm samples. Error bars represent standard deviations.

The experimental moving boundary layer position was calculated for the PVDF membranes fabricated with various particle sizes, shown in Figure 11. These figures show the linearized equation of the derived model (equation 13), with the slope of the model shown as a black line.

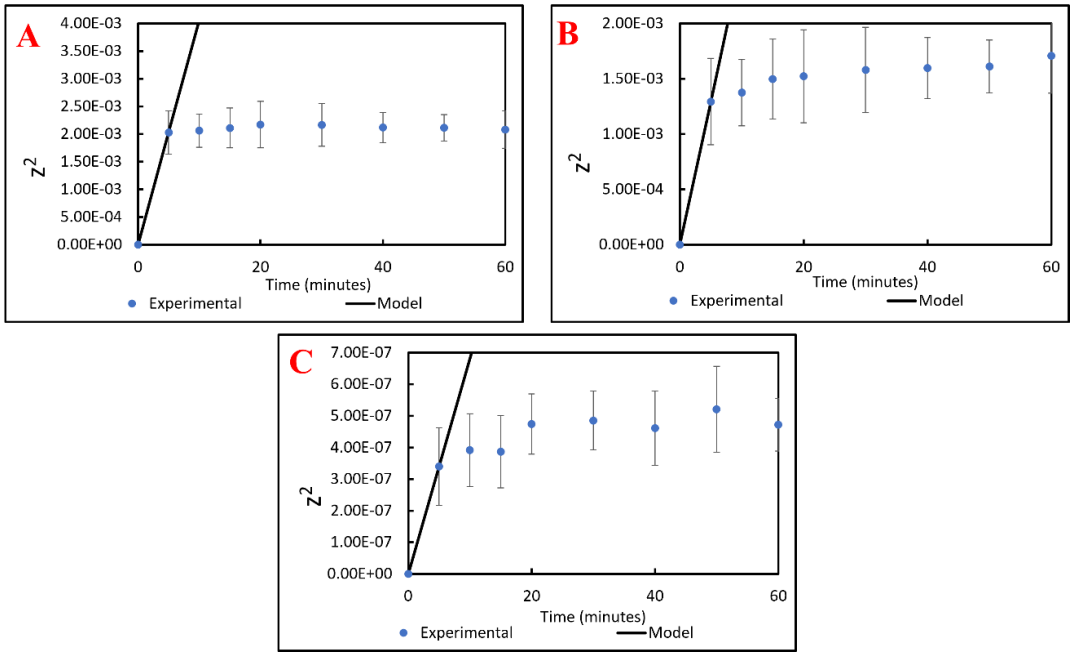

Figure 11. Experimental and Model Position of Moving Boundary Layer for Various Wt% ZnO Samples. A) The squared experimental moving boundary layer position of 35-45nm sized particles, with the black line representing the slope of the model equation. B) The squared experimental moving boundary layer position of 80-200nm sized particle samples, with the black line representing the slope of the model equation. C) The squared experimental moving boundary layer position for 500nm sized particles, with the black line representing the slope of the model equation. Each data point represents the average of four replicate trials in A, and three replicate trials for B and C, with error bars representing the standard deviation.

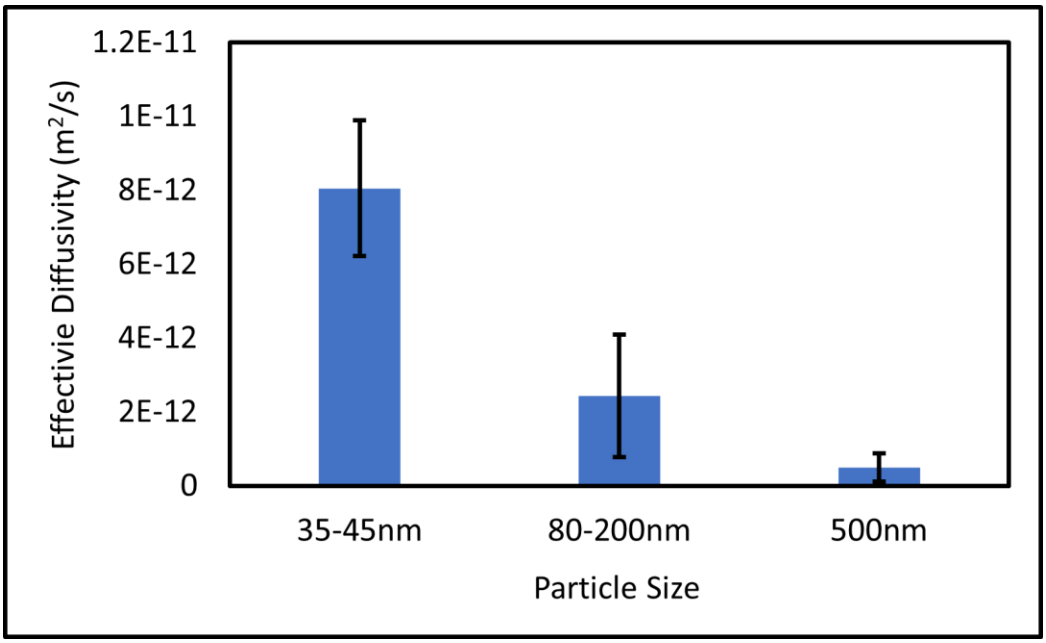

Figure 12. Effective Diffusivity of $ZnCl_2$ molecules through PVDF membranes of various particle sizes. The effective diffusivity of various wt% ZnO samples were calculated by using the slope of the model in figures 11A, B, and C. Each bar represents the average effective diffusivity of four replicates with error bars representing standard deviations.

The effective diffusivities were calculated using the slope of the model line in Figures 11A, B, and C, based on equation 13. The effective diffusivity decreased as the particle size increased. This suggests that the diffusion of $ZnCl_2$ occurs faster in samples with smaller particle sizes. These effective diffusivities cannot be used to estimate the diffusion coefficient. This is due to the fact that the model was only fit to data points where diffusion had occurred. Unfortunately, this meant that the model could only be fit to a single data point, which is not sound statistical methodology.

2.5) Discussion

The goal of this study was to optimize the ZnO removal from the PVDF matrix to produce PVDF sensors. A unimolecular diffusion equation was derived to model the diffusion of the $ZnCl_2$ from the PVDF membranes. The fraction of ZnO nanoparticles removed was calculated for each wt% and for various particle sizes. The trends for removal of ZnO nanoparticles were expected, but the derived model did not accurately predict the position of the moving boundary layer in the PVDF membranes. The derived model predicts the boundary layer should move closer and closer to the center of the membrane as more $ZnCl_2$ diffuses out of the PVDF matrix. The model did not predict the fast removal of ZnO as seen experimentally. The model predicted a slower-moving boundary layer as time increased in the acid bath, which was not seen experimentally.

It was observed that the fraction of ZnO removed from the membranes increased with increasing wt% ZnO and decreased with increasing particle sizes. The increase in fraction removed due to wt% ZnO could be caused by an increase in porosity. Both Roshani et al[31] and Ardeshiri[34] et al added modified ZnO nanoparticles to PVDF membranes to study the effects on filtration. These nanoparticles were kept inside the membrane, they were not removed after the casting process[31,34]. Roshani et al reported an increase in porosity and a decrease in tortuosity with increasing amounts of ZnO nanoparticles[31]. However, Ardeshiri et al reported decreasing porosity and increasing tortuosity with increasing amounts of nanoparticles[34]. These conflicting trends suggest more studies on how ZnO nanoparticles alter the porosity and tortuosity of PVDF membranes are needed. Even though both Roshani et al[31] and Ardeshiri et al[34] had conflicting porosity and tortuosity results, both described similar pore structures (“finger-

like" cavities) in the PVDF membranes. It is possible that the fabricated membranes in this study had similar structures, which could explain why some of the ZnO was dissolved in some samples, but not in others.

Both Roshani and Ardeshiri provided SEM images of the cross-sectional slices and surface images of ZnO-doped PVDF membranes, neither of which had surface pores[31,34]. If the fabricated PVDF membranes in this study had ZnO nanoparticles resting on the surface, it is possible that dissolving those nanoparticles would open up channels into the "finger-like" cavities described above. Both Roshani et al and Ardeshiri only added small amounts of ZnO to the membranes, up to 2% wt ZnO, compared to 10% wt ZnO samples fabricated in this study[31,34]. The larger amounts of ZnO nanoparticles increases the probability that the cavities could be turned into channels or pores, however, this is not guaranteed. This could explain why some samples had higher removal rates even within the same wt% groups.

The large tortuosity values reported by Ardeshiri et al suggest that there could be many channels formed in the PVDF membrane, yet they would not be interconnected[34]. The smallest tortuosity value reported was 7.18 for pure PVDF[34]. This means with no added ZnO to the membrane, the curvature of the pores were 7 times longer than the shortest distance between the ends of the pore. The addition of ZnO nanoparticles only increased the tortuosity in the membranes[34]. This would lead to many $ZnCl_2$ molecules being trapped inside the pores instead of diffusing out of the membrane. This is a possible reason, but unlikely for this study, since the samples were placed in the acid bath for 6 hours such that the ZnO nanoparticles were assumed to be dissolved. One way to confirm would be to leave samples in the acid bath for longer periods of time, such as 24 to 48 hours. Danley and Kloster reported that using the same fabrication protocol, not all ZnO was removed after being placed in the acid bath for 24 hours[26,36]. These two studies suggest that increasing the time in the acid bath might not improve the fraction of ZnO removed. Nevertheless, the tortuosity could be a factor for the low fraction of ZnO removed from the membranes.

For diffusion through a porous material, the effective diffusivity, D_e, is a function of the material's porosity, ε , and tortuosity, τ , of the PVDF membranes, as shown in equation 15:

$$D_e = D\frac{\varepsilon}{\tau} \quad (15)$$

The effective diffusivity of $ZnCl_2$ out of the PVDF membrane increased with higher wt% ZnO samples but decreased with larger particle sizes. This could be related to the fraction of ZnO removed from the membrane. One key observation in this study was that a majority of the $ZnCl_2$ diffused out of the membrane within 20 minutes in the acid bath. This limited the number of data points that could be used in the modeling calculations. The diffusion of $ZnCl_2$ could have been affected by the "finger-like" cavities observed in Ardeshiri and Roshani[31,34] or the reported large tortuosity values in Ardeshiri[34]. If the ZnO nanoparticles were grouped in large cavities in the membrane, and if a channel opened up to the cavity, the diffusion of $ZnCl_2$ out of the membrane would have occurred very rapidly. This would explain why the diffusion only occurred within the first 20 minutes. If the membranes were very tortuous, that could also explain why the effective diffusivities were smaller than expected. The expected diffusion coefficient value should be in the range of 10^{-9} m^2/sec for liquids[37], yet the largest effective diffusivity was calculated to be 8E-12 m^2/sec, which is three orders of magnitude smaller than expected.

A very tortuous membrane could have many pores that are not interconnected, meaning the $ZnCl_2$ would have a long distance to travel to diffuse out of the membrane. Since the samples were placed in an acid bath for 6 hours, it is possible that the membranes were very tortuous and the $ZnCl_2$ did not have enough time to diffuse out of the matrix. Extremely curved and twisted paths would lead to a decrease in diffusion in the PVDF membrane, which could explain what was observed experimentally.

The porosity and tortuosity of the membranes were not measured during this study, however, clearly these are important variables that need to be studied and characterized for further understanding of $ZnCl_2$ diffusion. Also, the fraction of ZnO removed from the PVDF membranes, the timing intervals, and the structure of the membranes should be investigated. Since a majority of the ZnO was removed within the

first five minutes, decreasing the time intervals between data acquisition would provide insight on the diffusion of the $ZnCl_2$ not seen in this experiment. Determining the porosity at each time interval along with final tortuosity measurements would allow for calculation of the diffusion coefficient rather than effective diffusivities.

Chapter 3) Calibrating PVDF Membranes for Use as a Biosensor in a Flow Chamber

3.1) Introduction

A flow chamber needs to be designed to calibrate PVDF membranes to investigate the complications of TAVR[6,38]. The PVDF sensor will track changes in pressure and flow patterns before and after implantation of the replacement heart valve. This flow chamber will need to mimic the flow rates and pressures produced by the heart.

Healthy blood pressure in an adult is defined as 120/80mm Hg[39]. The higher pressure refers to the peak pressure in the beat cycle, right after the heart beats (during systole)[39], while the lower pressure refers to the pressure in the aorta while the heart is resting in-between beats(during diastole)[39]. Johnson et al found that the pressure in patients prior to a TAVR procedure was 130mmHg/85mmg, while the pressure post-procedure dropped to 101mmHg/92mmHg[40]. They also reported that the blood flow rates changed from 162mL/s to 224mL/s for pre and post-implantation[40]. Flow rates were noted to increase from 270mL/s to 340mL/s after implantation while the patient was dosed with dobutamine[40], which is used during medical procedures when studying heart failures[41]. This means that the PVDF sensor should be able to detect changes in blood pressure from 80mmHg up to 130mmHg and flow rates from 162mL/s up to 340mL/s. To calibrate the PVDF sensor, a flow chamber was built to mimic these conditions.

3.2) Materials and Methods

A flow chamber was built to the dimensions of an aorta. The entire flow chamber can be seen below in Figure 13A. A Uniclife DEP-4000 submersible pump, circled in Figure 13B, was placed in a 30-gallon plastic tote, which was used as a water reservoir.

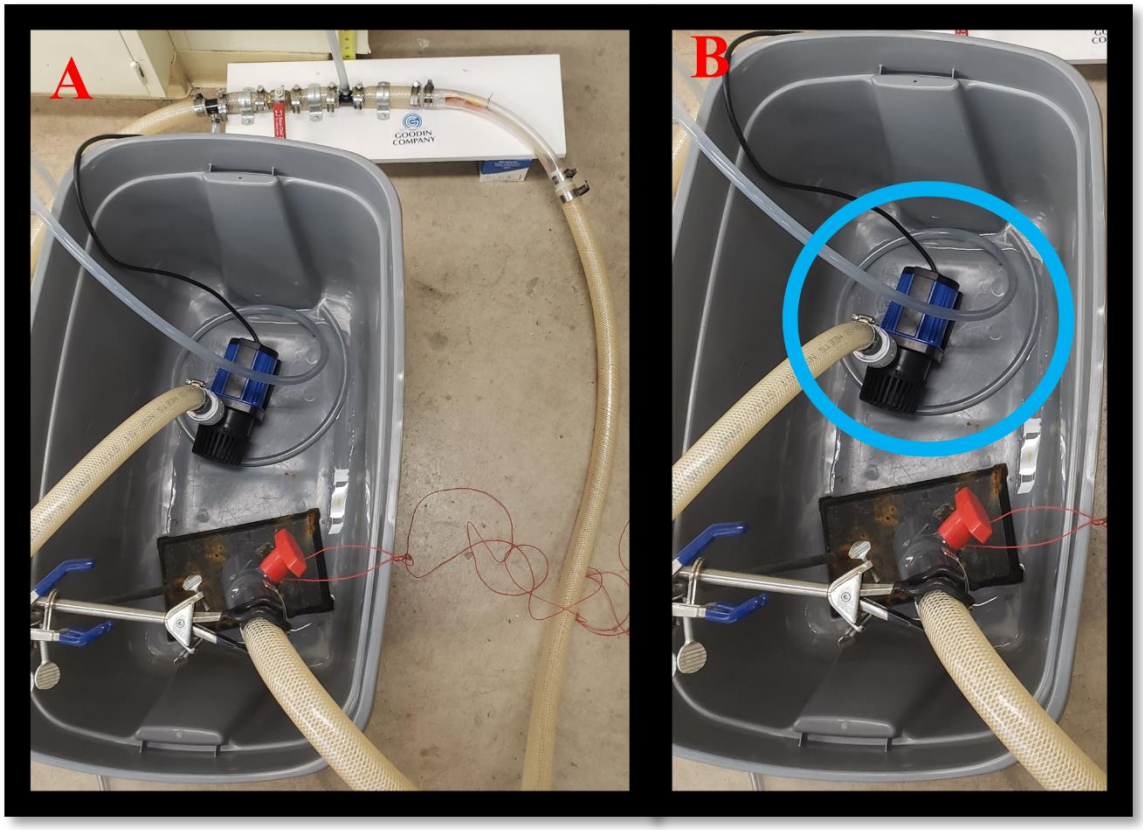

Figure 103. Flow Chamber. A) Whole flow chamber used to calibrate PVDF sensor. B) Uniclife DEP-4000 submersible pump circled in blue, inside the gray plastic tote, used as a water reservoir.

Water was fed through the submersible pump to a bypass valve. A bypass valve was added to the flow chamber to allow for water to be constantly running prior to diversion to the aortic segment with the PVDF sensor. This can be seen in Figure 14A. Pressure was measured using a manometer, shown in Figure 14A. The sensor was made by cutting a 1.5in X 1.5in square from a PVDF membrane (PolyK Technologies, State College, PA). The PVDF sensor had copper tape placed on either face of the membrane, with 0.5in strips placed on both faces to act as electrodes. Copper wire was used to hold alligator clips in place, which were connected to the electrodes on the PVDF sensor, illustrated in Figure 14 parts B and C. Figure 14B shows the PVDF sensor inside the aortic segment.

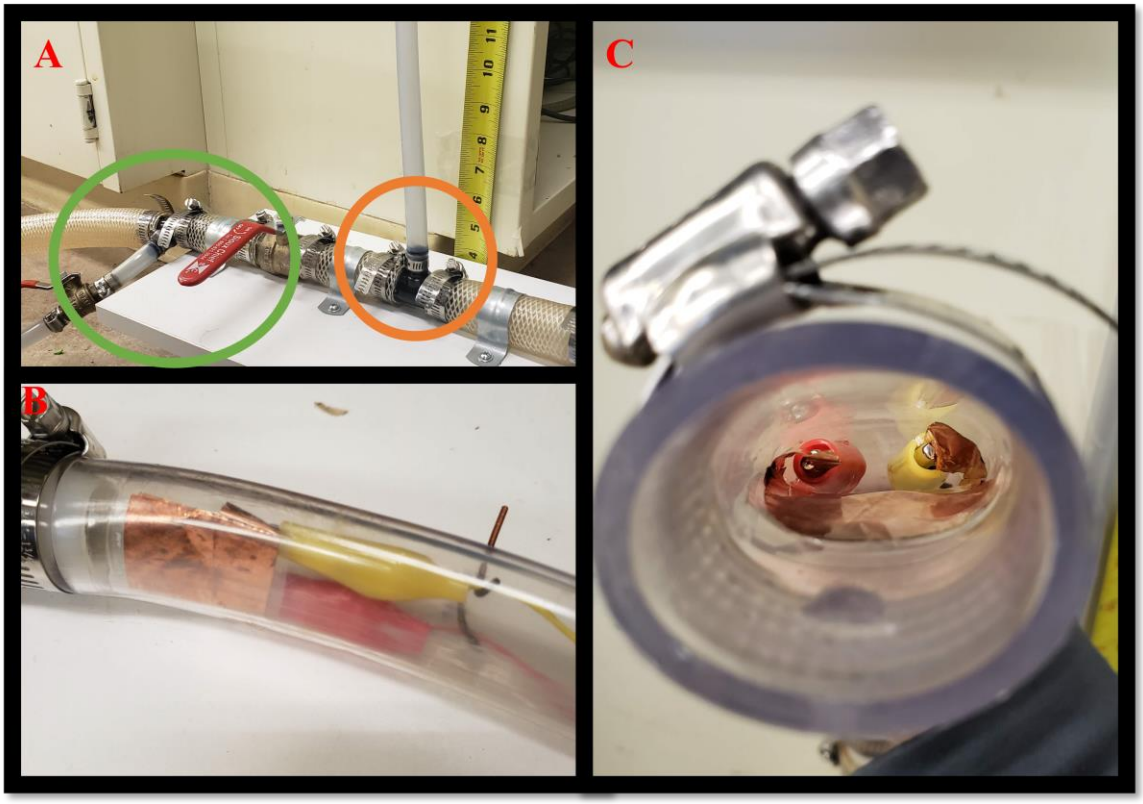

Figure 14. Bypass Valve, Manometer, and PVDF sensor. A) The bypass valve, circled in green, and tube used to direct flow away from the flow chamber along with a vertical tube, circled in orange, next to a tape measure that was used as a manometer to measure pressure. B) PVDF sensor in flow chamber held in place with alligator clips and copper wire. C) PVDF sensor resting on the wall of the flow chamber.

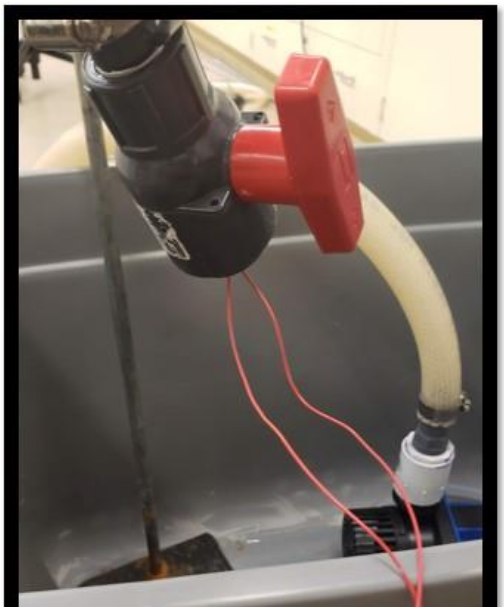

Figure 15. Return Hose Valve. The water exited out of the flow chamber through the return hose valve. The wire which was connected to the PVDF sensor is shown exiting the valve as well.

The alligator clips in Figure 14B and Figure 14C were connected to the wire, which was fed through the return hose, out the return valve, and to a National Instruments cDAQ-9174 chassis and NI 9215 input module. The wire is shown exiting the return hose in Figure 15, along with the return hose valve. The return hose valve was used to control the pressure in the flow chamber by restricting flow, thereby increasing the pressure.

The voltages generated from the PVDF sensor were measured using Labview software. The voltages were collected for 15

seconds at a rate of 100Hz for each flow rate and pressure test. Five different flow rates were used to calibrate the PVDF sensor, which corresponded to pump settings of 20, 40, 60, 80, and 100. Flow rate was determined by measuring the mass of the water ejected from a return hose that was collected in a graduated cylinder and timed using a stopwatch. Five replicates were collected at each pump speed with the return hose valve fully open. Then, five more replicates were collected with the return hose valve partially closed to maintain constant pressure in the flow chamber independent of the pump speed.

Data acquisition would start with the flow of water running through the bypass valve for three seconds. The initial three seconds were used as a baseline voltage reading. After three seconds, the flow of the water was directed toward the aorta segment with the PVDF sensor. The pressure in the flow chamber was determined by finding the height of the water in the manometer during each trial and subtracting the height of the water when there was no flow through the aorta segment. The raw voltage collected from Labview was filtered using a nine-point moving average. The response of the PVDF sensor was determined to be the blip in signal as shown by the black double-headed arrow, in Figure 16.

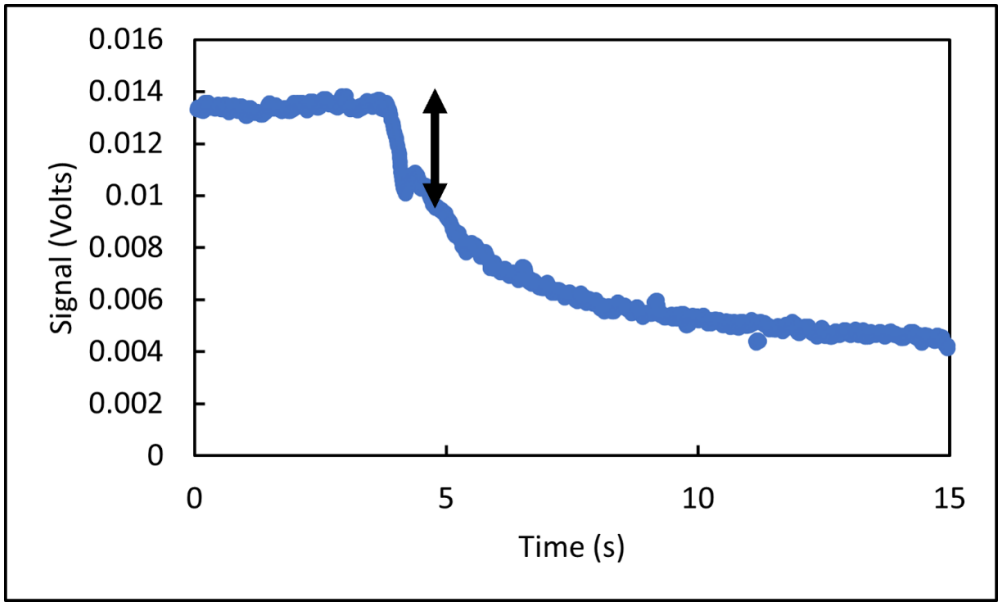

Figure 16. Sample Voltage collected from PVDF Sensor. This voltage from the PVDF sensor was collected under max flow rate. The black double-headed arrow shows the response of the PVDF sensor.

3.3) Results

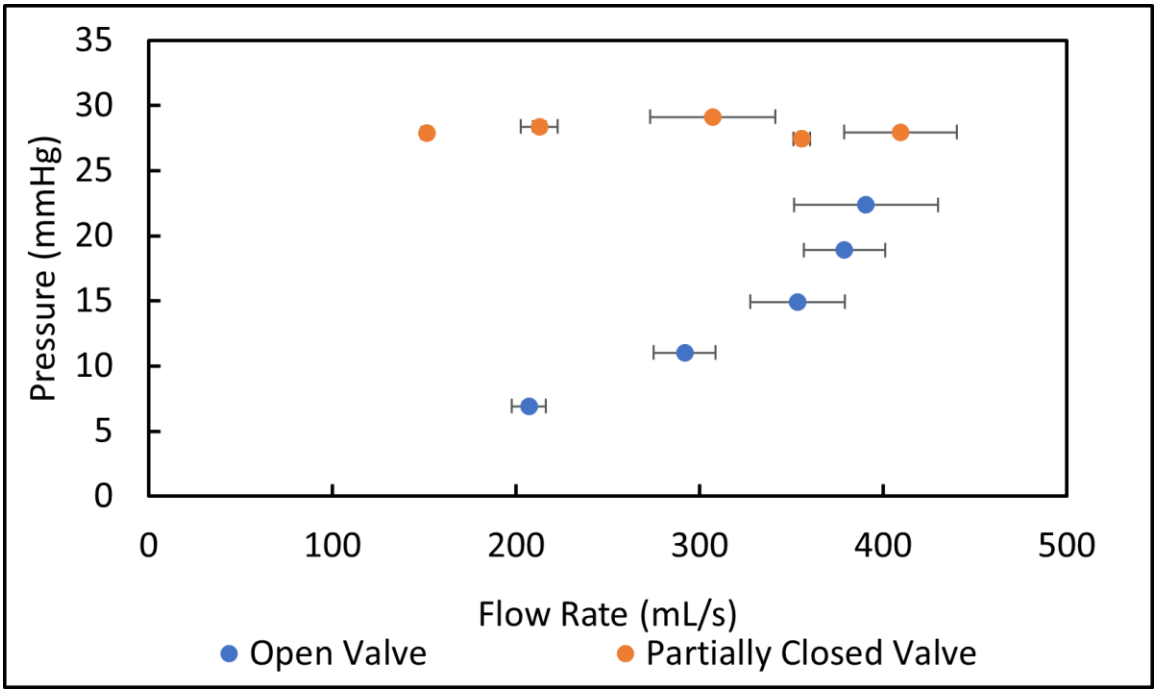

Figure 17. Flow Rates and Pressure Generated from Submersible Pump. The blue data points represent measurements collected with the return hose valve fully open. The orange data points represent measurements collected with the return hose valve partially closed. Error bars represent the standard deviation of five replicate trials.

Figure 17 shows the relationship between the flow rate of water and pressure in the flow chamber. With the valve open at the end of the return hose, the pressure increased with faster flow rates. With the valve partially closed, the pressure was held relatively constant while flow rates varied. This allowed for decoupling of the effect of flow rate and pressure on the signal obtained from the PVDF sensor in the flow chamber.

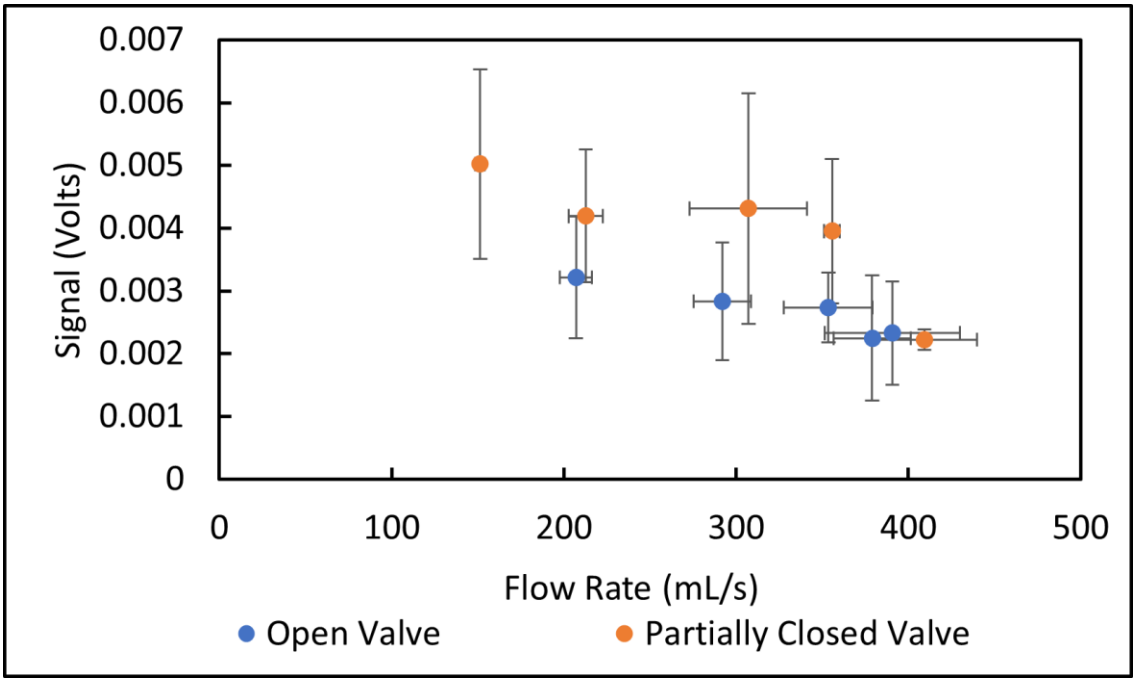

Figure 18. Flow Rate Compared to Signal Collected from PVDF Sensor. The blue data points represent trials with the return hose valve fully open, and the orange data points represent trials with the return hose valve partially closed. Each data point represents the average signal for five replicates. Error bars represent the standard deviation from each set of data collected.

Figure 18 shows the voltage signal acquired from the PVDF sensor versus the flow rates observed in the flow chamber. As the flow rates increased, the signal decreased for both the open valve trials and partially closed trials. The large standard deviations of each data point, however, suggest this downward trend is not statistically significant.

Figure 19 shows the voltage signal acquired from the PVDF sensor versus the pressure observed in the flow chamber. As the pressure increased for the open valve trials, the signal started to slightly decrease. Again, the large standard deviations of each data point suggest this trend is not statistically significant. The partially closed valve trials did not vary with pressure, but the voltage collected from the PVDF sensor were varied, as shown by the large standard deviations.

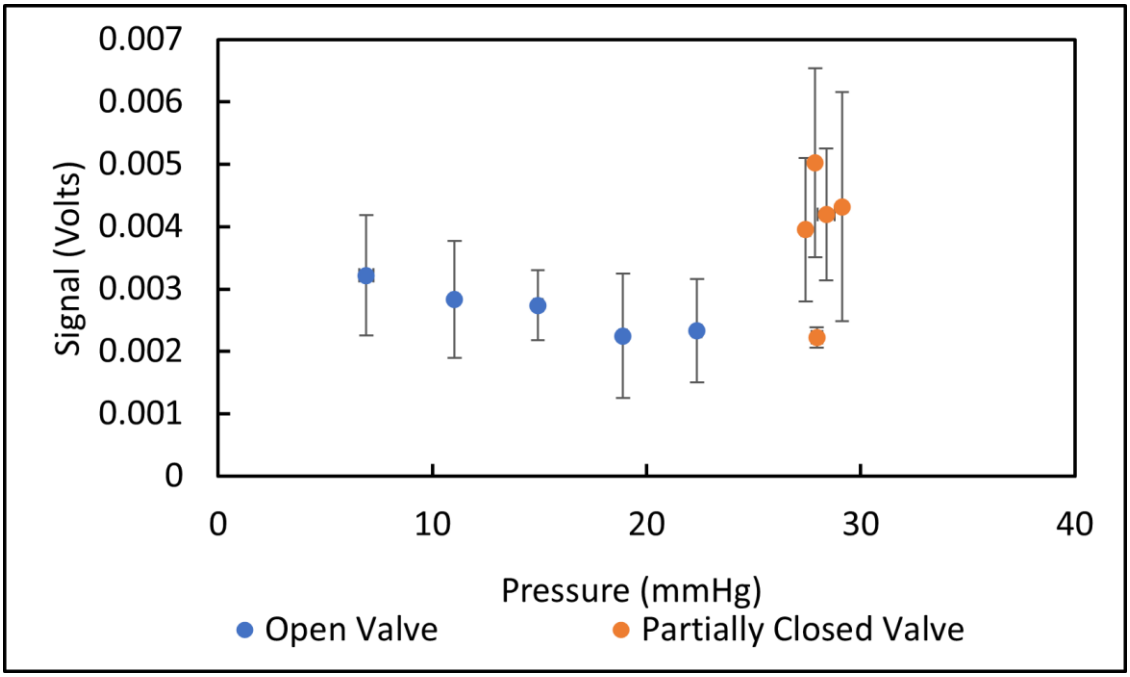

Figure 19. Pressure Compared to Signal Collected from PVDF Sensor. The blue data points represent trials with the return hose valve fully open, and the orange data points represent trials with the return hose valve partially closed. Each data point represents the average signal for five replicates. Error bars represent the standard deviation from each set of data collected.

3.4) Discussion

The trends of the voltage signal decreasing with both increasing pressure and flow rates were unexpected. Mao et al suggests that when the PVDF polymer chain is allowed to deform, it should produce a piezoelectric output[23]. It was thought that the higher flow rates and pressures would deform the PVDF polymer chains more than the low flow rates and pressures. The voltages collected from the PVDF sensor did not support this claim. One reason for this could be due to the low pressures found in the flow chamber, as the flow chamber did not perfectly mimic the conditions desired. The Uniclife submersible pump was able to provide flow rates of 150mL/s to 400mL/s, similar to those observed by Johnson et al[40] within the human aorta. However, the pump was not able to generate physiologically relevant pressures of up to 130mmHg in the flow chamber. Even with the return hose valve, the pressure did not increase to values seen inside the aorta[40]. It was thought that if the PVDF sensor could detect changes in lower pressures, presumably the membrane would be able to detect changes in higher pressure similar to physiological blood pressures, such as those reported by Johnson et al[40].

Under previous tests of the PVDF, the piezoelectric material generated larger voltages under very large pressures. The PVDF membrane from PolyK technologies was subjected to compression forces using a Test Resources Uniaxial tester. Figure 20 shows the increase in voltage from PVDF under compression up to 3000mmHg from this past study. This pressure is orders of magnitude larger than what is observed in the body, however, detectable signal was produced under pressures around 500mmHg. Extrapolating this trendline down to 100mmHg, which is around the pressure found in the body, the signal from PVDF would still be about 10 times larger than what was observed in this study.

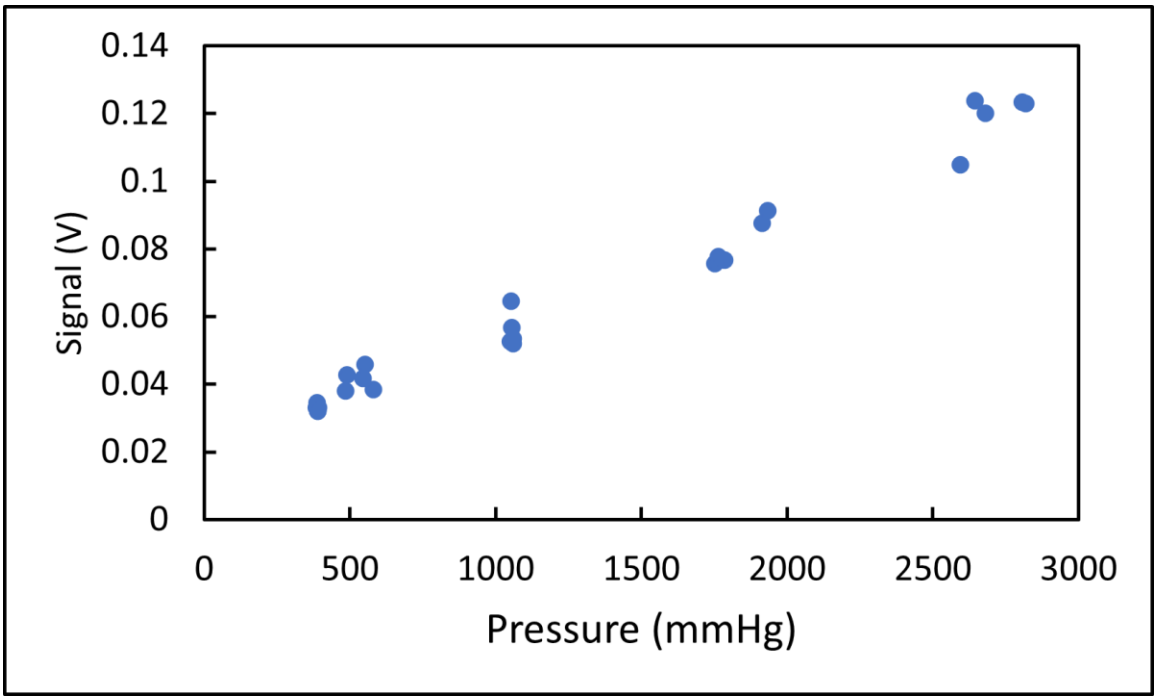

Figure 20. Voltage Generated from PVDF Membrane Using a Tensile Tester. The pressure applied from a tensile tester resulted in an increase in voltage from a PVDF membrane from previous studies[26].

PVDF has been shown to detect changes in flow velocity in a flow chamber[18]. Li reports that the piezoelectric signal increased with higher velocities in a flow chamber[18]. That trend was not observed in this study. When PVDF is used to detect changes in flow rates, it is measuring the changes in shear force on the surface of the membrane. Li et. Al measured the shear force of a fluid at velocities varying from 9 to 27m/s[18]. Velocities in the flow chamber varied from around 0.3m/s to about 0.8m/s. Li et al measured the shear force of air on PVDF membranes[18], while this experiment measured the shear force of

water on PVDF. The differences in fluid viscosities would lead to different shear forces on the PVDF membranes. This could explain the discrepancy in voltages observed in this study and those seen by Li et al[18]. Since the pressures in the flow chamber were lower than what would be expected in the aorta, solving the pressure issue is of utmost importance, however, further investigation into the shear forces should still be studied.

The pressures observed in the flow chamber were lower than the values reported by Johnson et al[40]. The pump used in the current setup is likely not adequate for calibrating the PVDF membrane and upgrading to a larger pump may solve this problem. PVDF has been shown to be a viable material as a biosensor measuring changes in pressure[22]. In a study by McLaughlin et. al, a PVDF sensor was placed outside the body on the arm to detect changes in pressure in the arteries for detecting pulse velocity[22], rather than inside the blood vessel as in this experiment. In addition, the authors used an amplifier during data acquisition, whereas no amplifier was used in this study[22]. Even so, they showed that PVDF can detect changes in pressure and is usable as a biosensor[22], which was not observed in these experiments.

One variable not studied in this experiment is how PVDF would detect changes in cyclic distension of the aorta. The hosing used in the flow chamber was thick plastic tubing. This hose did not flex once the water was allowed into the flow chamber. It is expected that a model silicone aorta will experience cyclic distension if a pulsatile pump is used, similar to that of a native aorta. This means if a PVDF sensor is connected to the surface of the silicone flow chamber, it would stretch and relax under pulsatile flow as the tube expands and contracts. Lei et al showed that PVDF can be used as a biosensor detecting changes in tension[21]. The PVDF sensor was placed on the chest of a patient and was used to monitor breathing, as the patient breathed in and expanded the chest, the PVDF sensor was subjected to tensile forces[21]. This cyclic distension variable will need to be studied, decoupled from the compressive and shear forces, and calibrated prior to investigating the complications of the TAVR procedure.

Chapter 4) Conclusion

PVDF has been shown to have applications as a biosensor[20,22,26]. Other studies have shown that instead of using bulk PVDF, inducing pores into the PVDF membrane can improve piezoelectric output[23,25]. Porous PVDF membranes have not been optimized and calibrated for use as a biosensor, and not specifically for flow and pressure studies inside a flow chamber. The goals of this study were to optimize one variable in the fabrication process and to calibrate bought PVDF in a flow chamber.

The optimization of ZnO removal in PVDF membranes during the fabrication process was partially achieved. Trends in the fraction of ZnO nanoparticles removed suggest there is an optimal porosity and particle size for fabricating PVDF membranes with additional pores and minimal amounts of residual ZnO. The derived unimolecular model did not accurately predict the position of the moving boundary layer, which suggests additional variables in the diffusion process. These variables may include homogeneity, porosity, and tortuosity.

To calibrate the PVDF sensors, a flow chamber was built to mimic the conditions found in the aorta. The flow chamber was able to reach physiological flow rates, but not physiological blood pressures. Since the observed pressure was significantly lower than expected, the PVDF sensor was unable to be calibrated. However, PVDF has been shown to generate detectable voltages when compressed with large forces. Increasing the pressure in the flow chamber with a larger submersible pump should theoretically allow for calibration of the PVDF sensors.

Going forward, the ZnO removal process needs optimization to increase the fraction removed and diffusion of $ZnCl_2$ out of the membrane. Ardeshiri et al[34] and Roshani et al[31] observed changes in porosity and tortuosity of PVDF membranes with the addition of ZnO nanoparticles. Designing methodology to determine the porosity and tortuosity at each time interval could improve the modeling of $ZnCl_2$ out of the matrix.

As discussed in Chapter 3, using a larger pump that generates more pressure could allow for calibration of PVDF sensors inside the aorta segment. Previous experiments show that PVDF generates detectable signal under physiologically relevant pressures

while under compression using a tensile tester. Once the PVDF sensor is calibrated in the current flow chamber apparatus, studying the effects of the TAVR in vitro using a silicone replica of the aorta is possible.

Bibliography

(1) *Transcatheter aortic valve replacement (TAVR) - Mayo Clinic*. https://www.mayoclinic.org/tests-procedures/transcatheter-aortic-valve-replacement/about/pac-20384698 (accessed 2021-06-22).

(2) *TAVR vs SAVR: Comparing Transcatheter & Surgical Aortic Valve Replacement*. https://healthblog.uofmhealth.org/heart-health/tavr-vs-savr (accessed 2021-07-19).

(3) *Aortic valve stenosis - Symptoms and causes*. Mayo Clinic. https://www.mayoclinic.org/diseases-conditions/aortic-stenosis/symptoms-causes/syc-20353139 (accessed 2022-07-04).

(4) Team, H. J. Aortic Stenosis Causes, Symptoms, Diagnosis, Treatment & Surgery. *Health Jade*, 2019.

(5) *Aortic Stenosis Overview*. www.heart.org. https://www.heart.org/en/health-topics/heart-valve-problems-and-disease/heart-valve-problems-and-causes/problem-aortic-valve-stenosis (accessed 2021-08-05).

(6) Culler, S. D.; Cohen, D. J.; Brown, P. P.; Kugelmass, A. D.; Reynolds, M. R.; Ambrose, K.; Schlosser, M. L.; Simon, A. W.; Katz, M. R. Trends in Aortic Valve Replacement Procedures Between 2009 and 2015: Has Transcatheter Aortic Valve Replacement Made a Difference? *The Annals of Thoracic Surgery* **2018**, *105* (4), 1137–1143. https://doi.org/10.1016/j.athoracsur.2017.10.057.

(7) Himbert, D.; Vahanian, A. Transcatheter Aortic Valve Replacement for Patients with Heart Failure. *Heart Failure Clinics* **2015**, *11* (2), 231–242. https://doi.org/10.1016/j.hfc.2014.12.003.

(8) *How TAVR Devices Work - Transcatheter Aortic Valve Replacement (TAVR)*. www.bostonscientific.com. https://www.bostonscientific.com/en-US/patients/about-your-device/tavr-devices/how-tavr-devices-work.html (accessed 2022-07-21).

(9) Kolte, D.; Khera, S.; Vemulapalli, S.; Dai, D.; Heo, S.; Goldsweig, A. M.; Aronow, H. D.; Elmariah, S.; Inglessis, I.; Palacios, I. F.; Thourani, V. H.; Sharaf, B. L.; Gordon, P. C.; Abbott, J. D. Outcomes Following Urgent/Emergent Transcatheter Aortic Valve Replacement. *JACC: Cardiovascular Interventions* **2018**, *11* (12), 1175–1185. https://doi.org/10.1016/j.jcin.2018.03.002.

(10) Gleason, T. G.; Reardon, M. J.; Popma, J. J.; Deeb, G. M.; Yakubov, S. J.; Lee, J. S.; Kleiman, N. S.; Chetcuti, S.; Hermiller, J. B.; Heiser, J.; Merhi, W.; Zorn, G. L.; Tadros, P.; Robinson, N.; Petrossian, G.; Hughes, G. C.; Harrison, J. K.; Conte, J. V.; Mumtaz, M.; Oh, J. K.; Huang, J.; Adams, D. H. 5-Year Outcomes of Self-Expanding Transcatheter Versus Surgical Aortic Valve Replacement in High-Risk Patients. *Journal of the American College of Cardiology* **2018**, *72* (22), 2687–2696. https://doi.org/10.1016/j.jacc.2018.08.2146.

(11) Mazzella, A. J.; Hendrickson, M. J.; Arora, S.; Sanders, M.; Li, Q.; Vavalle, J. P.; Gehi, A. K. Shifting Trends in Timing of Pacemaker Implantation After

Transcatheter Aortic Valve Replacement. *JACC: Cardiovascular Interventions* **2021**, *14* (2), 232–234. https://doi.org/10.1016/j.jcin.2020.09.034.

(12) Eirin, A.; Lerman, A.; Lerman, L. O. Mitochondrial Injury and Dysfunction in Hypertension-Induced Cardiac Damage. *Eur Heart J* **2014**, *35* (46), 3258–3266. https://doi.org/10.1093/eurheartj/ehu436.

(13) Valverde, I.; Gomez, G.; Coserria, J. F.; Suarez-Mejias, C.; Uribe, S.; Sotelo, J.; Velasco, M. N.; Soto, J. S. D.; Hosseinpour, A.-R.; Gomez-Cia, T. 3D Printed Models for Planning Endovascular Stenting in Transverse Aortic Arch Hypoplasia. *Catheterization and Cardiovascular Interventions* **2015**, *85* (6), 1006–1012. https://doi.org/10.1002/ccd.25810.

(14) Haghiashtiani, G.; Qiu, K.; Zhingre Sanchez, J. D.; Fuenning, Z. J.; Nair, P.; Ahlberg, S. E.; Iaizzo, P. A.; McAlpine, M. C. 3D Printed Patient-Specific Aortic Root Models with Internal Sensors for Minimally Invasive Applications. *Sci. Adv.* **2020**, *6* (35), eabb4641. https://doi.org/10.1126/sciadv.abb4641.

(15) Jo M. Zelis; Meiburg, R.; Jorn Roijen; Koen Janssens; Marcel Veer; Nico Pijls; Nils Johnson; Frans de Vosse; Pim Tonino; Marcel Rutten. 3D-Printed Stenotic Aortic Valve Model to Simulate Physiology before, during, and after Transcatheter Aortic Valve Implantation | Elsevier Enhanced Reader. *International Journal of Cardiology 313* (2020), 32–34. https://doi.org/10.1016/j.ijcard.2020.04.087.

(16) Sharma, T.; Aroom, K.; Naik, S.; Gill, B.; Zhang, J. X. J. Flexible Thin-Film PVDF-TrFE Based Pressure Sensor for Smart Catheter Applications. *Ann Biomed Eng* **2013**, *41* (4), 744–751. https://doi.org/10.1007/s10439-012-0708-z.

(17) Nurettin Sezer. A Comprehensive Review on the State-of-the-Art of Piezoelectric Energy Harvesting. *ResearchGate*.

(18) Li, Q.; Xing, J.; Shang, D.; Wang, Y. A Flow Velocity Measurement Method Based on a PVDF Piezoelectric Sensor. *Sensors* **2019**, *19* (7), 1657. https://doi.org/10.3390/s19071657.

(19) Chen-Glasser, M.; Li, P.; Ryu, J.; Hong, S. Piezoelectric Materials for Medical Applications. In *Piezoelectricity - Organic and Inorganic Materials and Applications*; Vassiliadis, S. G., Matsouka, D., Eds.; InTech, 2018. https://doi.org/10.5772/intechopen.76963.

(20) Takashima, K.; Horie, S.; Mukai, T.; Ishida, K.; Matsushige, K. Piezoelectric Properties of Vinylidene Fluoride Oligomer for Use in Medical Tactile Sensor Applications. *Sensors and Actuators A: Physical* **2008**, *144* (1), 90–96. https://doi.org/10.1016/j.sna.2008.01.015.

(21) Lei, K.-F.; Hsieh, Y.-Z.; Chiu, Y.-Y.; Wu, M.-H. The Structure Design of Piezoelectric Poly(Vinylidene Fluoride) (PVDF) Polymer-Based Sensor Patch for the Respiration Monitoring under Dynamic Walking Conditions. *Sensors* **2015**, *15* (8), 18801–18812. https://doi.org/10.3390/s150818801.

(22) McLaughlin, J.; McNeill, M.; Braun, B.; McCormack, P. D. Piezoelectric Sensor Determination of Arterial Pulse Wave Velocity. *Physiol. Meas.* **2003**, *24* (3), 693–702. https://doi.org/10.1088/0967-3334/24/3/306.

(23) Mao, Y.; Zhao, P.; McConohy, G.; Yang, H.; Tong, Y.; Wang, X. Sponge-Like Piezoelectric Polymer Films for Scalable and Integratable Nanogenerators and Self-Powered Electronic Systems. *Adv. Energy Mater.* **2014**, *4* (7), 1301624. https://doi.org/10.1002/aenm.201301624.

(24) Tucker, J. A.; Danley, M. J.; Kloster, J. T.; Zhao, P.; Lai, V. K. Effect of Fabrication Conditions on the Performance of Porous Polyviny- Lidene Fluoride (PVDF) Piezoelectric Sensors under Compression. *Cur Res Mater Chem* **2021**, *3* (1). https://doi.org/10.33790/crmc1100110.

(25) Yan Zhang; Chris R. Bowen; Sylvain Deville. Ice-Templated Poly(Vinylidene Fluoride) Ferroelectrets. *Soft Matter 2019* (15), 825–832. https://doi.org/10.1039/c8sm02160k.

(26) Danley, M. Characterization of Spongelike Porous Polyvinylidene Fluoride (PVDF) for Use as a Biosensor, University of Minnesota.

(27) Zhaolin Gao. Characterization of Nanoporous Polyvinylidene Fluoride (PVDF) Sensors under Tensile Loading, University of Minnesota.

(28) Zhaolin Gao; Matthew Danley; Jack T. Kloster; Victor Lai; Ping Zhao. Characterization of Nanoporous Polyvinylidene Fluoride (PVDF) Sensors Under Tensile Loading. In *Proceedings of the ASME 2021 Conference on Smart Materials*; 2021.

(29) Jack Kloster; Matthew Danley; Tony Struntz; Victor Lai; Ping Zhao. SIMULATING THE EFFECTS OF POROSITY ON THE D31 PIEZOELECTRIC COEFFICIENT OF POLYVINYLIDENE FLUORIDE. In *Proceedings of the ASME 2022 Conference on Smart Materials, Adaptive Structures and Intelligent Systems SMASIS2022*; 2022.

(30) *PVDF piezoelectric film, 28um/45um/120 um thick, Thick Screen-Printed Silver Electrode, energy harvesting, piezo sensor*. Piezoelectric & Pyroelectric PVDF & PVDF-TrFE, Resin, Film, Sensor, Transducer, and Test Instrument. https://piezopvdf.com/pvdf-piezoelectric-film-thick-silver-ink/ (accessed 2021-08-18).

(31) Ramin Roshani; Fatemeh Ardeshir; Peyravi, M.; Mohsen Jahanshahi. Highly Permeable PVDF Membrane with PS/ZnO Nanocomposite Incorporated for Distillation Process. *Royal Society of Chemistry* **2018**, *2018* (8), 23499–23515. https://doi.org/10.1039/c8ra02908c.

(32) *Membranes and Filter Papers for Western Blotting | Thermo Fisher Scientific - US*. https://www.thermofisher.com/us/en/home/life-science/protein-biology/protein-assays-analysis/western-blotting/transfer-proteins-western-blot/membranes-transfer-buffers-western-blotting.html (accessed 2021-08-16).

(33) *Immun-Blot® PVDF Membrane*. Bio-Rad Laboratories. https://www.bio-rad.com/en-us/product/immun-blot-pvdf-membrane?ID=9f95f7dc-8ad2-4923-8eb4-be822b64e2f4 (accessed 2022-08-24).

(34) Ardeshiri, F.; Salehi, S.; Peyravi, M.; Jahanshahi, M.; Amiri, A.; Rad, A. S. PVDF Membrane Assisted by Modified Hydrophobic ZnO Nanoparticle for Membrane Distillation. *Asia-Pacific Journal of Chemical Engineering* **2018**, *13* (3), e2196. https://doi.org/10.1002/apj.2196.

(35) H. Scott Fogler. Mass Transfer Limitations in Reacting Systems. In *Elements of Chemical Reaction Engineering*; Prentice Hall.

(36) Jack T. Kloster. Computational and Experimental Comparison of the Effects of Porosity on the Piezoelectric Characteristics of Polyvinylidene Fluoride (PVDF) Thin Films, University of Minnesota.

(37) Ismail Tosun. *Modeling in Transport Phenomena*, Second Edition.; Elsevier Science and Technology Books, 2007.

(38) Cormican, D.; Jayaraman, A.; Villablanca, P.; Ramakrishna, H. TAVR Procedural Volumes and Patient Outcomes: Analysis of Recent Data. *Journal of Cardiothoracic and Vascular Anesthesia* **2020**, *34* (2), 545–550. https://doi.org/10.1053/j.jvca.2019.04.016.

(39) *Understanding Blood Pressure Readings*. www.heart.org. https://www.heart.org/en/health-topics/high-blood-pressure/understanding-blood-pressure-readings (accessed 2022-07-14).

(40) Johnson, N. P.; Zelis, J. M.; Tonino, P. A. L.; Houthuizen, P.; Bouwman, R. A.; Brueren, G. R. G.; Johnson, D. T.; Koolen, J. J.; Korsten, H. H. M.; Wijnbergen, I. F.; Zimmermann, F. M.; Kirkeeide, R. L.; Pijls, N. H. J.; Gould, K. L. Pressure Gradient vs. Flow Relationships to Characterize the Physiology of a Severely Stenotic Aortic Valve before and after Transcatheter Valve Implantation. *European Heart Journal* **2018**, *39* (28), 2646–2655. https://doi.org/10.1093/eurheartj/ehy126.

(41) *DOBUTamine Monograph for Professionals*. Drugs.com. https://www.drugs.com/monograph/dobutamine.html (accessed 2022-07-14).